Applied Thermal Engineering 217 (2022) 119180

Contents lists available at ScienceDirect

Applied Thermal Engineering

journal homepage: www.elsevier.com/locate/apthermeng

Research Paper

Analysis of an energy storage system using reversible calcium hydroxide in fluidised-bed reactors

O. Bartoli [a,b], R. Chacartegui [a,d,*], A. Carro [a], C. Ortiz [c], U. Desideri [b], J.A. Becerra [a,d]

[a] Dpto. Ingeniería Energética, Universidad de Sevilla, Camino de los Descubrimientos s/n, 41092 Sevilla, Spain
[b] Department of Energy, Systems, Territory and Construction Engineering, University of Pisa, Largo Lucio Lazzarino 1, Pisa 56122, Italy
[c] Materials and Sustainability Group, Department of Engineering, Universidad Loyola Andalucía, Avda. De las Universidades s/n, 41704 Dos Hermanas, Seville, Spain
[d] Universidad de Sevilla, Laboratory of Engineering for Energy and Envorinmental Sustainability, 41092 Seville, Spain

ARTICLE INFO

Keywords:
Thermochemical Energy Storage
Calcium Hydroxide
Calcium Oxide
Fluidised Bed Reactor
Solar energy

ABSTRACT

The widespread use of renewable energy requires the support of high-capacity energy storage systems. This work proposes a thermochemical energy storage system for concentrated solar power plants based on the reversible hydration/dehydration process of the calcium hydroxide. It is a single fluidised bed reactor concept with alternating dehydration-hydration processes, charging and discharging alternating reactions, with superheated steam as fluidising agent. The system has been modelled using Aspen Plus™, including equilibrium data and hydrodynamic performance of the reactor. The model has been used to evaluate the effect of different parameters of the reactor, such as geometry, average particle size, or inlet streams conditions, on the performance of the reactor and the system. The thermal integration of the system was optimised using pinch analysis. For the proposed layouts, round-trip efficiencies values of 68 % are obtained. The economic analyses show specific investment costs between 4170 $/kWe and 3250 $/kWe for plants in the range of 31 MW to 45 MW, which are competitive with those expected for plants with storage of molten salts in this power range. LCOE values between 67 $/MWh and 83 $/MWh were obtained. The analyses show how these values highly depend on the fresh material replacement requirements related to the deactivation of the material and operational strategies. The results show the interest in further developments of this concept for concentrated solar power plants.

1. Introduction

Increasing the share of renewable energy sources worldwide is crucial to reducing greenhouse gas emissions and mitigating climate change. Due to the inherent intermittency of renewables, such an increase in production requires the development of large-scale storage capacities. In this context, thermal energy storage systems (TES) are key technologies to balance supply and demand fluctuations [1].

Concentrated solar power (CSP) plants are key renewable technologies due to their capability to integrate thermal energy storage [3]. These thermal storage technologies can be classified according to the physics of the heat storage and release: sensible, latent, and thermochemical[2]. The most extended energy storage technology in CSP plants is the molten salt technology based on sensible heat storage. It is successfully operative at a commercial scale. Still, it has challenges. Storage material costs are approximately 50 % of the total energy storage system. Corrosion-related challenges affect integration and durability [4,5] and their operating temperature range is constrained to 200–600 °C to avoid salt solidification and degradation, respectively [6]. There is an intense research activity for alternatives to molten salts to improve some of their characteristics [7]. Latent storage systems exploit polycrystalline materials (PCMs) that absorb or release thermal energy through a phase transition [8]. Studies on PCMs show that it is possible to store around ten times more heat than sensible systems [9]. However, both physical heat storage systems (sensible and latent) are not suitable for long-term storage due to thermal losses related to their nature. Thermochemical storage systems (TCES) are emerging as an alternative to large-scale thermal energy storage [10]. TCES use reversible chemical reactions to store and release thermal energy. Energy is accumulated in chemical bonds during the endothermic reaction (charging phase) and released during the exothermic reaction (discharging phase). The main advantage of TCES is that long storage periods can be expected, as long as the components can be stored without losing their chemical potential [11]. Different reversible chemical reactions have been proposed for thermochemical energy storage, each

* Corresponding author.
E-mail address: ricardoch@us.es (R. Chacartegui).

https://doi.org/10.1016/j.applthermaleng.2022.119180
Received 6 May 2022; Received in revised form 15 July 2022; Accepted 15 August 2022
Available online 17 August 2022

Nomenclature

η_{RT}	Round-Trip Efficiency
η_{PB}	Power Block Efficiency
η_{tot}	Overall system efficiency
χ_{HY}	Solids Conversion During Hydration Reaction
χ_{DEHY}	Solids Conversion During the Dehydration Reaction
ξ	Ratio between the thermal power spent to preheat the water from the storage tank to the superheated reactor inlet conditions and the thermal power available from the reactor. All considered during hydration
v	The ratio of the steam flow rate reacted to the total steam flow rate entering the reactor during hydration.
τ	Average residence time of particles in the fluidised bed
N_{Ca}	Number of moles in fluidised bed
F_{Ca}	Molar flow rate of solid entering the fluidised bed
d_p	Particle diameter
$T_{solidin}$	Temperature of the solid input to the reactor [K]
$T_{Reactor}$	Reactor temperature [K]
T_{gasin}	Temperature of gas that enters the reactor [K]
$\dot{m}_{gasin}$	Gas mass flow incoming to the reactor [kg/s]
$\dot{m}_{vap}$	Steam mass flow incoming to the reactor [kg/s]
$\dot{m}_{solidin}$	Solid mass flow incoming to the reactor [kg/s]
m_{HTF}	Heat transfer fluid (compressed air) [kg/s]
$p_{Reactor}$	Reactor pressure [bar]
$D_{Reactor}$	Reactor diameter [m]
$H_{Reactor}$	Reactor height [m]
H_{inlet}	Insertion height of solid [m]
H_{outlet}	Solid output height [m]
$D_{Cyclone}$	Cyclone diameter [m]
d_t	Tube diameter [m]
a	Distance between tubes [m]
L_t	Tube length [m]
N_s	Number of layers
N_t	Number of tubes
CC	Capital investment cost $[\frac{\$}{kW}]$
$O\&M_{fix}$	Fix operation and maintenance cost $[\frac{\$}{kW\ yr}]$
$O\&M_{var}$	Variable operation and maintenance cost $[\frac{\$}{kWh}]$
CF	Capacity Factor
F_{cost}	Fuel cost $[\frac{\$}{MM\ Btu}]$
HR	Heat rate $[\frac{Btu}{kWh}]$

Abbreviations

TES	Thermal energy storage
CSP:	Concetrated Solar Power
TCES:	Thermochemical energy storage
PCM:	Phase-change material
FB:	Fluidised bed
HY:	Hydration reaction (discharge phase of the system)
DEHY:	Dehydration reaction (charging phase of the system)
HY-1/2:	Hydration reaction for the first/second integration study
DEHY-1/2:	Dehydration reaction for the first / second integration study
HTF:	Heat Transfer Fluid (compressed air at 15 bar)
PSD:	Particle size distribution
LCOE:	Levelized cost of electricity $[\frac{\$}{MW_h}]$
ESD_{eff}:	Effective Energy Storage Density $ESD_{eff} = \frac{Q_{HY}}{F_{CaO} \cdot \frac{M_{CaO}}{\rho_s} 3.6} [\frac{kWh}{m^3}]$
GCC:	Grand Composite Curve
BCC:	Balanced Composite Curve

characterised by its temperature range, reaction energy and states of reactants and products [12].

Among the most promising TCES for large-scale applications are the systems based on calcium hydroxide, Ca(OH)2. The system is based on the reversibility of endothermic dehydration of $Ca(OH)_2$ and exothermic hydration of CaO (Eq. (1)). Its reaction enthalpy is approximately 109 kJ/mol, and the application temperature range is between 700 and 1000 K [13]. The concept is based on abundant non-toxic and low-cost materials and good reversibility of the reactions. Steam is used as the fluidising agent. It can be handled and stored efficiently. The discharge temperatures are in the range of 600 °C, which allows the integration of mature power technologies, such as the Rankine cycle.

$$Ca(OH)_{2(s)} \leftrightarrow CaO_{(s)} + H_2O_{(v)} \quad \Delta H_{reaction} = 109\,\mathrm{kJ/mol} \tag{1}$$

Calcium hydroxide, such as TCES, has been proposed focusing on applications such as solar thermal power [26], process heat [14], heat pumps [15] or engine preheating [16]. Its use as energy storage has also been studied at the laboratory level [17,18]. These studies include different reactors: fixed bed reactors [13], small-scale fluidised bed reactors [19,20], plate exchange reactors [21] or moving bed reactors [22]. Schmidt et al. [18] developed a 10 kW proof of concept of a novel thermochemical reactor based on calcium hydroxide. Several strategies were experimentally analysed, using the exothermic step to heat air to 450 °C. Another experimental reactor was carried out by Cosquillo et al. [22]. They developed a moving-bed reactor filled with $CaO/Ca(OH)_2$ with ceramic shell and Al_2O_3 nanostructured particles, which improved the cyclability and conversion properties of the materials. Xu et al. [23] evaluated the influence of material porosity for both direct and indirect heating strategies. Different authors have analysed the thermal cycling stability of the process. Dai et al. [24] found that after 20 cycles, there was no performance degradation, a favourable characteristic compared to deactivation in carbonate-based TCES systems [25]. However, agglomeration and poor thermal conductivity are challenging for the technology deployment [24].

The integration of CSP-TCES using calcium hydroxide technology for large-scale storage applications has only been partially studied. Bayon et al. [26] presented a techno-economic evaluation of solid–gas TCES systems for solar thermal applications, considering three plant models with a reference power of 100 MWe: a reference plant with molten salt storage, a closed loop cycle, and an open cycle. Thermal efficiency of 98.5 % was obtained by integrating a calcium hydroxide energy storage system, with a small parasitic consumption and a capital cost of 4.78 $/MJ. For molten salts presented values of 9.61–16.78 $/MJ. Criado et al. [27] studied a thermochemical energy storage process based on $CaO/Ca(OH)_2$ in a single circulating fluidised bed reactor coupled to large solid storage silos. In the base case, with a maximum thermal power of 100 MWth during hydration, a thermal efficiency (thermal to thermal) of the process of 63 % was obtained. Tapaches et al. [28] proposed a CSP storage system based on the $Ca(OH)_2/CaO$ reaction, using a single fixed bed reactor integrated with a Rankine steam cycle and estimated costs in the range of 12–60 €/MWh, depending on the location considered in the plant. Pelay et al. presented the energy and exergy analysis [29] and the LCA [30] of the integration of CSP-TCES with Rankine cycle power cycles through the conceptual study of three different configurations from a base case of a 100 MW_e solar tower plant. Overall efficiency (thermal to electrical) values in the range of 34.9–39.2 % were obtained.

Based on these promising results, new designs and integration schemes are needed to advance the integration of the calcium hydroxide-based TCES system in CSP plants. This work proposes and analyses a new integration layout of calcium hydroxide thermochemical storage system. It is based on a single fluidised bed reactor (FB) integration for both the charging and discharging steps that operate

sequentially. The concept simplifies plant integration and reduces costs. On the other hand, the design of the FB reactor requires special attention to ensure adequate performance in both operating stages. The present work analyses technology integration in CSP plants, and provides novel insights regarding the predesign of the reactor (FB) and the thermal integration of the systems. From a detailed assessment of the reaction and reactor conditions, equilibrium data, kinetics, and hydrodynamic performance of the FB reactor, the study delves into the potential integrations with the CSP plant, comparing operation strategies for both atmospheric and pressurised reactor configurations. Thermal integration has been optimised by the pinch analysis technique, maximising system performance with the temperature difference between reaction (450–600 °C) and storage temperature [31,32]. Key parameters associated with the FB reactor are discussed from the sensitivity analysis, such as reactor temperature and pressure, particle size, gas velocity, conversion, and reactor volume. The analysis is complemented with a detailed economic study and estimation of economic indicators. These analyses provide key design insights for integrating calcium hydroxide-based FB TCE systems in CSP plants.

2. Calcium hydroxide as TCES

This section details the model of the calcium hydroxide system, including equilibrium data, reaction kinetics, and hydrodynamic performance in the FB reactor.

The reactor model is based on the thermodynamic equilibrium of the chemical reaction. The equilibrium curves have been determined experimentally by different authors. Schaube et al. evaluated the start of dehydration and rehydration for a range of steam pressures from 4.3 kPa to 95.6 kPa [33], while Samms and Evans determined the equilibrium curve between 100 and 5000 kPa [34] This work uses the equilibrium curve data from the work of Barin [35] (Eq. (2)). Fig. 1 represents the equilibrium curves of these experimental works.

$$Ln\left(P_{eq}\right) = -\frac{11607}{T_{eq}} + 19.254 \tag{2}$$

Equilibrium curves show that high temperatures and low steam pressures favour the dehydration reaction. It highlights a specific operational challenge for the charging stage. According to the suggestion of Criado et al. [36], if the fluidised bed operates at atmospheric pressure, the corresponding equilibrium temperature (following the Barin equilibrium curve and in continuity with [36]) is about 792 K. It provides one criterion for integrating dehydration reactions. Atmospheric pressure reactors must operate with temperatures above 792 K. The integration of this experimental model assures reliable numerical results regarding the development of reactions within the reactor at this level.

Regarding the chemical reaction kinetics, hydration and dehydration reactions have been experimentally shown to be first-order reactions [37]. Different reactors have been used to simulate the behaviour of the thermochemical system in the laboratory. Fuji presented an air-heated reactor [14]. Schaube et al. demonstrated the operation in a fixed-bed

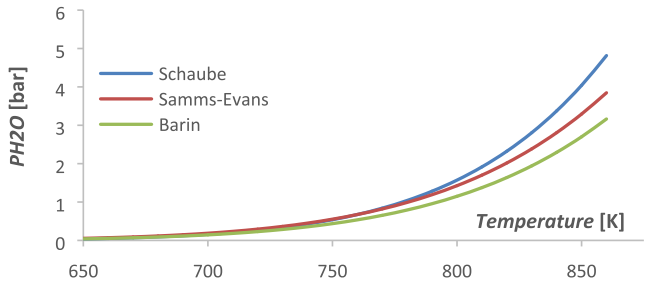

Fig. 1. Equilibrium curves proposed in the literature: Shaube [33], Samms and Evans [34] and Barin [35].

reactor, in which material (60 g) was in direct contact with nitrogen gas and steam mixture. Twenty-five dehydration and rehydration cycles were carried out at different partial steam pressures: 17.6, 35.5, 74.1 and 95.6 kPa [13]. Pardo et al. performed the reaction in a fluidised bed reactor using a mixture of $Ca(OH)_2$ and an inert to facilitate the fluidisation [20]. Ogura et al. presented a reactor with indirect heating [38]. Schmidt et al. [21] used a 10 kW_{th} plate exchange reactor prototype, where with a 20 kg of solids inventory conversions of 77 % were achieved with no material degradation. Recently, Cosquillo et al. [39] developed a 1 kW_{th} moving-bed reactor where solid particles fall from the top to the bottom while reacting with steam, using a transfer fluid for the heat exchange. Rougé et al. [19] simulated the behaviour of a 4 kW_{th} fluidised bed prototype, processing up to 20 kg/s of solid particles. Based on these experimental results, it is possible to develop models at higher scales and estimate the performance of large-scale plants with different layouts and operation modes.

As reported in [40], the reaction rate depends on the difference between steam volume fraction v_{H2O} (Eq. (4)) and equilibrium volume fraction $v_{H2O,eq}$ (Eq. (3)).

$$v_{H2O,eq} = \frac{p_{eq}}{p_{reactor}} = \frac{2.3 \cdot 10^{8} exp\left(-\frac{11607}{T}\right)}{p_{reactor}} \tag{3}$$

$$v_{H2O} = \frac{p_{H_2O\ \ operative,inlet}}{p_{reactor}} \tag{4}$$

Most of the studies have considered fixed-bed reactors. The typical configuration is the shell and tube, in which the inventory of solids remains static inside the exchanger. Steam is alternately extracted or supplied to the reactor [41,42]. Although good results have been achieved, these reactor types present substantial limitations, mainly due to the low heat exchange coefficients achieved. In addition, the renewal of fresh solid material, caused by the expected reversibility loss due to the intrinsic cyclic degradation, seems complicated with a packed bed configuration. A fluidised bed configuration can solve these issues.

This work analyses a FB reactor operation with Aspen Plus™ software under steady-state conditions, considering well-isolated adiabatic components and an isothermal reactor. The gas velocity in the reactor is calculated by Eq. (5).

$$u_{gas} = \frac{V_{gas}}{A_{bed}} \tag{5}$$

where V_{gas} is the volumetric flow of the fluidising agent, A_{bed} is the cross-sectional area of the reactor.

The minimal fluidisation condition appears when the drag force of the gas is equal to the weight of the bed of particles. The drag force is equal to the product between the pressure drop through the bed and the cross-sectional area of the bed. The Ergun equation connects them (Eq. (6)).

$$\frac{\Delta p}{h_{mf}} = \frac{\rho_g u^2 \left(1-\varepsilon_{mf}\right)}{\varphi d_p \varepsilon_{mf}} \left[\frac{150\left(1-\varepsilon_{mf}\right)\mu}{\rho_g d_p u} + 1.75\right] \tag{6}$$

where h_{mf} is the bed height under the minimum fluidisation conditions when the bed of particles are static. The overall balance of forces becomes as in Eq. (7).

$$\Delta p A_{bed} = A_{bed}\ h_{mf}\ \left(1-\varepsilon_{mf}\right)\ \left(\rho_s - \rho_g\right)\ g \tag{7}$$

Combining equations (4) and (5), the value of the minimum fluidising velocity u_{mf} solving Eq. (8).

$$1.75\frac{1}{\varepsilon_{mf}}\frac{1}{\varphi}\left(\frac{d_p u_{mf}\rho_g}{\mu}\right)^2 + 150\frac{1-\varepsilon_{mf}}{\varepsilon_{mf}^3\varphi^2}\frac{d_p u_{mf}\rho_g}{\mu} = \frac{dp^3\rho_g\left(\rho_s-\rho_g\right)g}{\mu^2} \tag{8}$$

For a velocity higher than ten or more u_{mf} a greater amount of particles is dragged in the freeboard region according to the mean diameter of the particles which form the bed: some return to the bed while others

evolve outside the reactor with the gas. For estimating the terminal velocity (u_t) this work uses the relation proposed by Haider and Levenspiel [43] (eq. (9))[43].

$$u_t = u_t^* \left(\frac{\mu(\rho_s - \rho_g)g}{\rho_g^2} \right)^{\frac{1}{3}} \tag{9}$$

where u_t^* is a dimensionless quantity calculated as:

$$u_t^* = \left(\frac{18}{Ar^{\frac{2}{3}}} + \frac{2.335 - 1.744\ \varphi_s}{Ar^{\frac{1}{6}}} \right)^{-1} \tag{10}$$

[44].

3. $Ca(OH)_2/CaO$ thermochemical energy storage integration

A sequential modelling approach has been implemented to evaluate the overall performance of the system from the reactor performance, the thermal integrations, and the economic analysis (Fig. 2). The conceptual layout of the system is presented in Fig. 3. It is considered the base case for the study of the performance of the fluidised bed reactor in dehydration and hydration processes to define adequate performance conditions for integrating a single fluidised bed for hydration and dehydration reactions. The fluidised bed reactor temperature will be maintained using a heat transfer fluid (HTF). A design criterion is to lower the charging temperature of the system as much as possible. This can be achieved by changing the partial pressure of the steam. The fluidisation gas can be diluted with inert gas, where air is used to keep the reactor at atmospheric pressure and decrease steam pressure. In the present study, nitrogen gas as a diluent was also considered to avoid possible undesirable carbonation reactions between CO_2 in air and CaO. This choice also allows for a reduction in pressure and consequent operation with lower reactor temperatures. Still, it requires the insertion of a separator between incondensable N_2 and steam downstream of the reactor to operate in a closed loop. This solution is disregarded as it introduces a greater complexity to the plant layout and higher installation and operating costs, although in future integrations under different layouts could be of interest.

The discharge phase of the system (hydration reaction) occurs to the left of the equilibrium curves, Fig. 1, and is promoted at low temperatures and high steam pressures. The temperature during the heat release phase is lower than the required for the charging phase under the same pressure for both reactions. Based on the equilibrium curve [35], operating temperatures around 743 K are needed in an atmospheric pressure reactor for a sufficient degree of hydration reaction.

Two thermal integrations of the thermochemical storage system within an integrated solar power plant and a steam power cycle are considered. They differ in the discharge and reactor strategies: the first integration operates with a fluidised bed at a pressure close to atmospheric pressure, and the second with a fluidised bed pressurised at 6 bar, Fig. 4. An indirect thermal integration for the reactor was adopted, using compressed air at 15 bar as the heat transfer fluid of the receiver. Air was chosen as the working fluid to avoid the possibility of residues being formed on the walls of the heat exchanger tubes, where the heat transfer fluid and steam will alternately evolve. The residues could be dragged by the steam during the discharge phase of the system, with consequent damage to the turbine blades. The solar receiver chosen is a volumetric metal foam type [41]. Hydration and dehydration reactions operate for 12 h each, and system dynamics during stage inversion are neglected, although a transition period will appear in practice. The analyses and results of this work are valid under steady-state conditions.

The layout of the charging stage system is the same for both integrations (Fig. 5). Hot air from the solar receiver maintains the fluidised bed at a temperature of 800 K and heats, evaporates, superheats, and then reheats for the power cycle. The heat exchangers network provides thermal coupling between the hot and cold currents of the system, recovers heat, and avoids the need for external heating units. The hot solids leaving the reactor are stored at the reactor outlet temperature. It allows using these hot solids during the next step, thus reducing the heating loads [36]. The condenser operating at a temperature of 322.1 K and a pressure of 0.1 bar is cooled using air coolers.

The layouts of the two integrations related to the hydration phase differ in a turbine downstream of the reactor. In the case of the pressurised reactor, Fig. 6b, energy is recovered by expanding excess steam that has not been involved in the hydration reaction [41]. The stored water must be heated, evaporated, and superheated to reach the necessary hydration reaction conditions before entering the fluidised bed. It requires a tank with these capacities. Heat recovery is possible from solids that leave the reactor to increase efficiency.

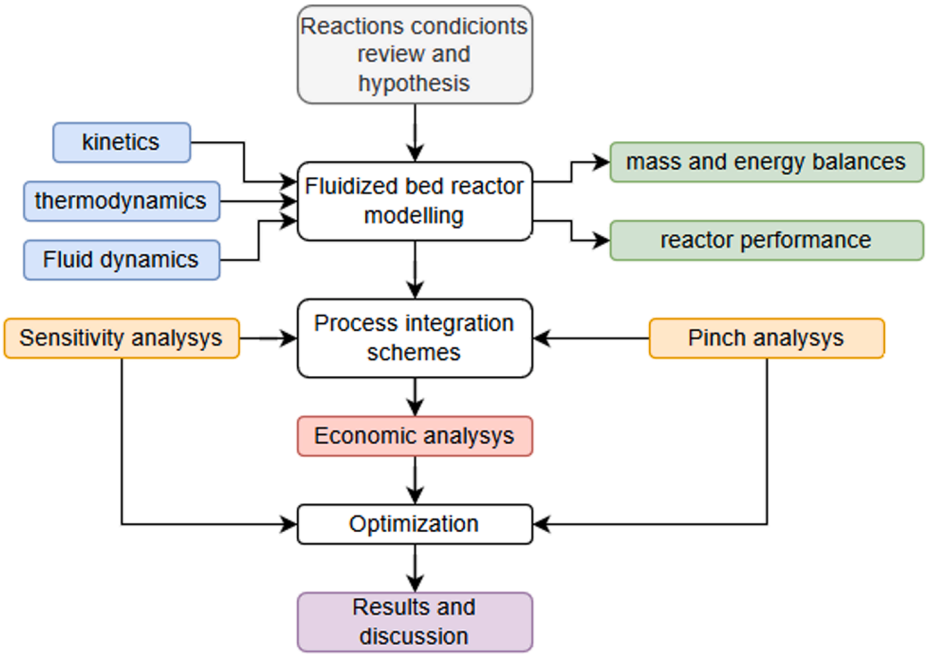

Fig. 2. Modelling methodology followed in this work.

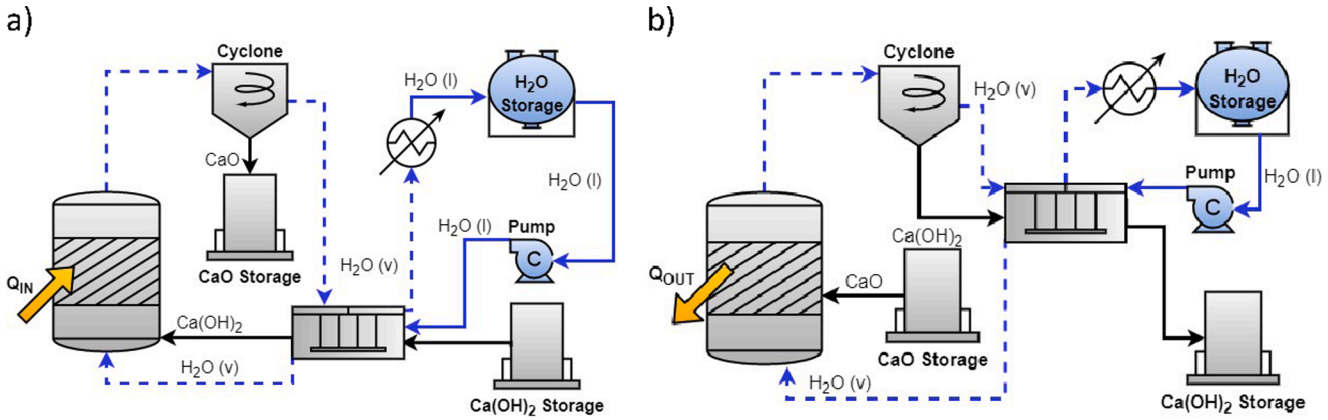

Fig. 3. Conceptual scheme for: a) Dehydration looping process layout; b) Hydration looping process layout.

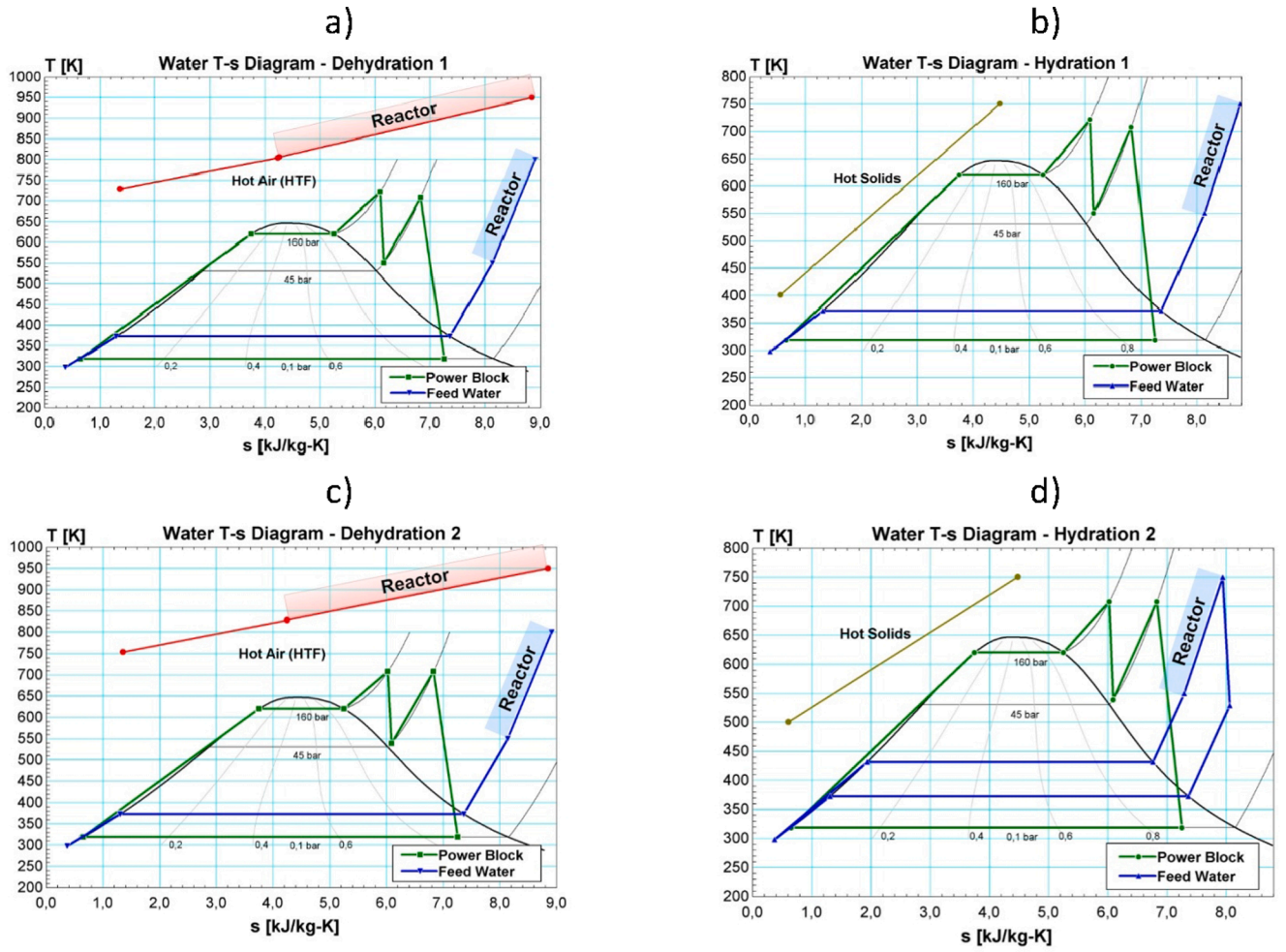

Fig. 4. *T*-s diagram for a) Dehydration 1st thermal Integration; b) *T*-s diagram for Hydration 1st thermal Integration; c) Dehydration 2nd thermal Integration; d) *T*-s diagram for Dehydration 2nd thermal integration.

4. Process simulation and analysis

Process simulation is carried out using Aspen Plus™. The analysis is oriented to assess the estimated performance of the system in terms of solid conversion and heat available during the charging and discharging phases. Table 1 presents the ranges of the parameters used in the analysis.

The simulation conditions were presented in previous sections. The reactor model is based on the thermodynamic equilibrium of the chemical reaction, using thermochemical data for the equilibrium curve from the work of Barin [35]. The reactor operation is simulated with Aspen Plus™ software under steady-state conditions, considering well-isolated adiabatic components and an isothermal reactor. Fluid dynamics and reactor operation conditions for both charging and discharging stages were discussed in Sections 2 and 3, respectively. The NRTL-RK model (Non-Random-Two-Liquid) was used to simulate the

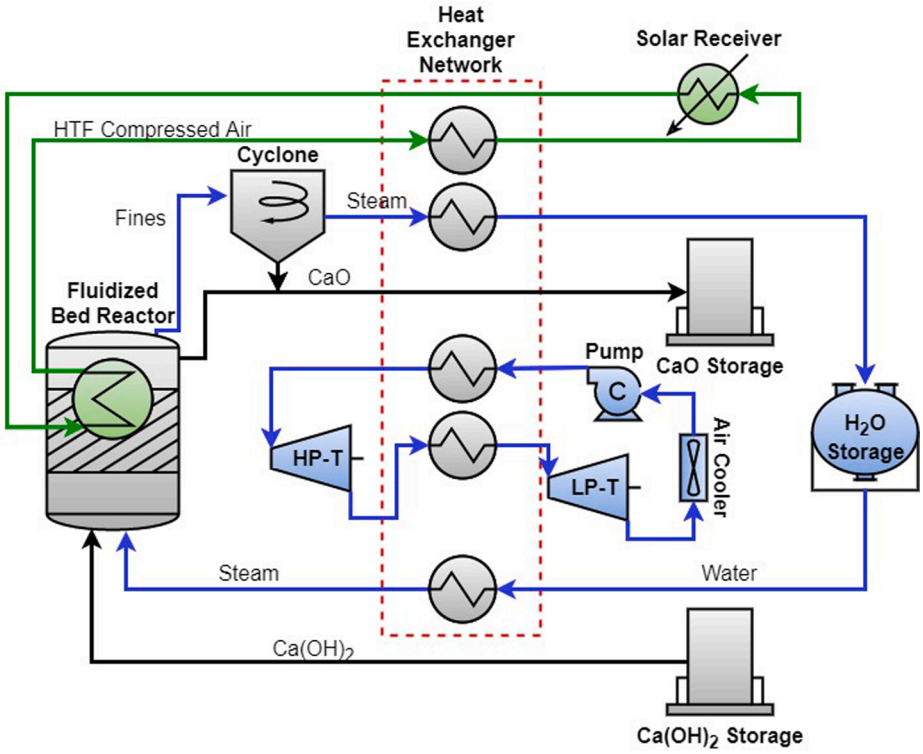

Fig. 5. Process flow diagram for the d*ehydration* stage.

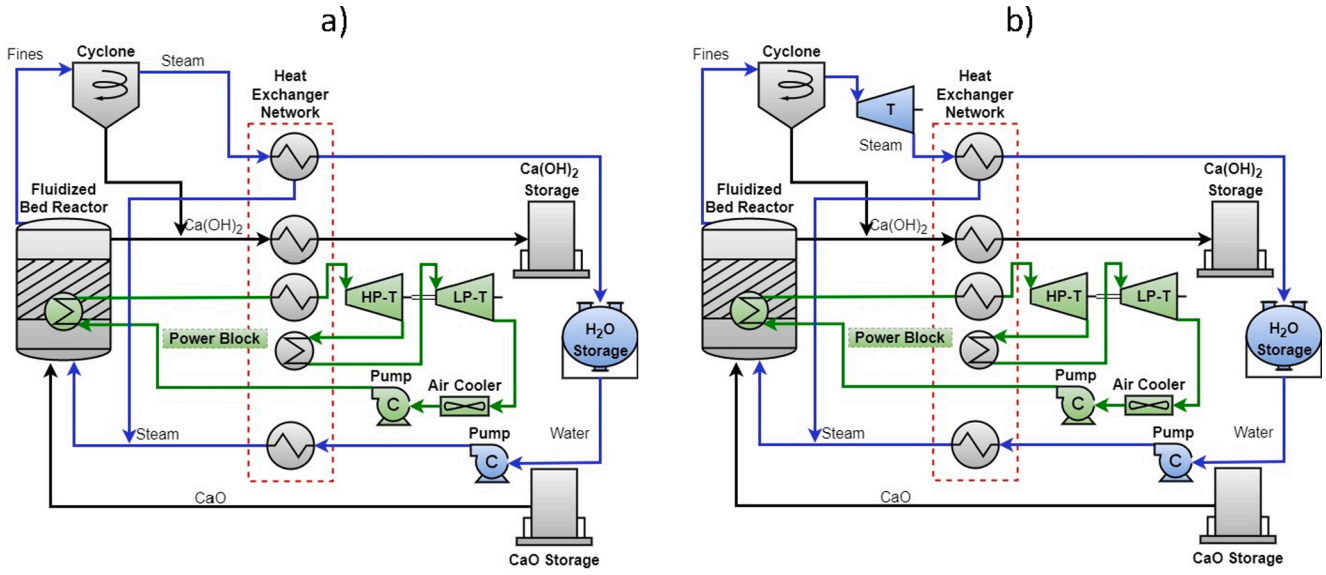

Fig. 6. Process flow diagram for the hydration stage: a) Atmospheric FB reactor (HY-1); b) Pressurised FB reactor -6 bar- (HY-2).

solid–gas reaction in the reactor, using the Redlich-Kwong equation of state for the steam phase. The downstream cyclone of the reactor, which provides solid–gas separation, is a Stairmand-HT type with the calculation method based on the model suggested by Muschelknautz et al. [44].

4.1. *Dehydration stage*

The effect of the particle size in the dehydration process was evaluated for different height/diameter ratios of the reactor, Fig. 7. It shows that almost complete dehydration is expected in all cases.

Small particles (50 μm) have high conversion rates due to improved kinetics but are easily transported with the gas out of the reactor, being fluidisation operation more challenging. Particles with large diameters reduce the efficiency of the reactor with lower conversion values. For the presentation of the subsequent analyses, an intermediate particle size of 200 μm was selected, with a stable and efficient reactor behaviour.

The charging phase of the system achieves almost complete conversion at temperatures above 750 K. Fig. 8 shows the conversion degree as a function of the temperature for different aspect ratios of the reactor.

For the ranges of particle sizes and temperatures analysed, the impact of the geometry of the fluidised bed reactor is almost irrelevant as far as the chemistry of the reaction is concerned. Still, it has

Table 1
Values of the parameter used for the analysis of hydration and dehydration.

Parameter	Units	Hydration	Dehydration
		Range	
d_p	μm	50–700	50–700
$T_{solid\ in}$	K	300–700	300–800
$T_{Reactor}$	K	550–870	600–900
$\dot{m}_{gas\ in}$	kg/s	27–60	1–30
$p_{Reactor}$	bar	1–6	1
$D_{Reactor}$	m	6–12	5–11
$H_{Reactor}$	m	5–20	5–12
Threshold		*Value*	
$\dot{m}_{solid\ in}$	kg/s	100	100
$T_{gas\ in}$	K	>400	>400
H_{inlet}	m	10%$H_{Reactor}$	10%$H_{Reactor}$
H_{outlet}	m	90%$H_{Reactor}$	90%$H_{Reactor}$
$D_{Cyclone}$	m	3	3

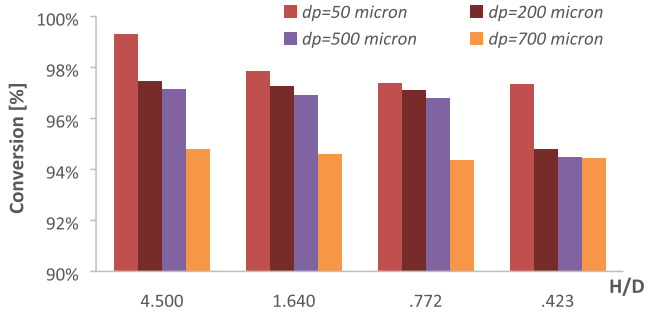

Fig. 7. Effect of particle size on dehydration conversion for different Height/Diameter ratios (V = 441.8 m^3).

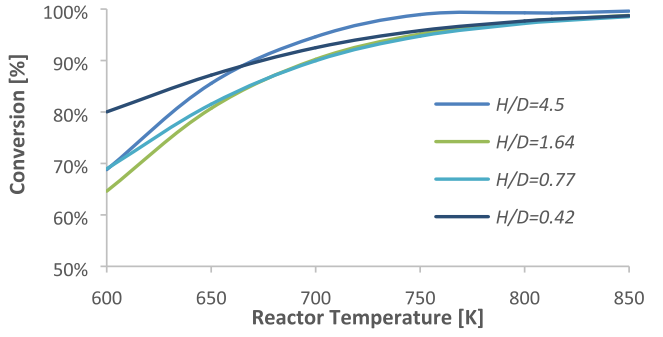

Fig. 8. Solid conversion versus temperature of the reactor for a FB volume of 441.8 m^3.

noticeable effects on the fluidised bed fluid dynamics. For larger reactors, the flow of solid particles out of the fluidised bed decreases, Fig. 8. Besides the impact on the reactor through successive cycles, having relevant values of solids in the outflow stream would penalise the performance of the cyclone and the separation of solids and gases.

During the dehydration phase, high inlet steam flow rates reduce the conversion of solids. For the selected geometry, a steam flow rate of 2.5 kg/s was imposed based on the model in Section 2, assuring fluidification conditions in the analysed range. Steam must be produced from water stored at ambient temperature, and a reduction in the flow rate reduces heat requirements, improving performance during the charging phase. Fig. 9 shows the solids in the outflow stream as a function of the diameter of the reactor for the fixed steam flow.

Fig. 9 shows that operating at the same $Ca(OH)_2$ flow rate, reactors with larger diameters decrease the transport effect of solid particles

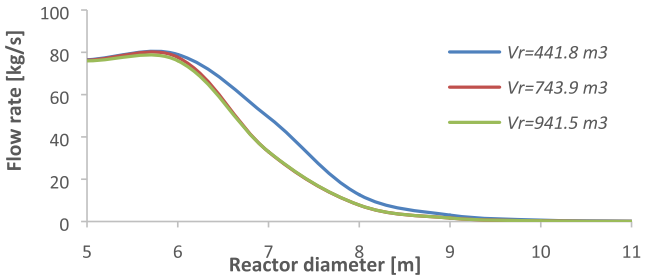

Fig. 9. Solids transported outside the reactor as a function of reactor diameter.

outside the fluidised bed. Fig. 10 shows the gas velocities at the reactor inlet and outlet. Low and wide reactors require lower inlet fluid velocities than those used in high and narrow reactors. The dehydration reaction of $Ca(OH)_2$ leads to an increase in the value of the gas velocity at the reactor outlet compared to that at the inlet. This effect increases the possibility of transporting solid particles out of the reactor.

4.2. Hydration stage

Unlike dehydration, the hydration reaction is less effective, making it challenging to achieve conversion values up to 80 % for reactors at ambient pressure. The reaction is favoured at high temperatures. Fig. 11 shows the conversion rates obtained for different reactor temperatures and different steam flow rates. For the reference geometry, steam flows of 30 kg/s led to high CaO conversion values.

The hydration reaction is affected by the size of the reactor. As the volume of the reactor increases, both the conversion value and the heat released by the reactor increase. A larger reactor volume leads to greater contact between the solid and gaseous particles; increasing the contact surface between the gas bubbles and the emulsion phase increases the exchange of matter, so the reaction is favoured. Fig. 12 shows the conversion fraction with a reactor temperature of 750 K, and the steam temperature and the CaO inlet temperature at 550 K. Fig. 12 shows that each reactor configuration has a maximum solid conversion fraction, varying from 0.33 to 0.65 in a volume range between 441.8 m^3 and 1406.6 m^3. These results are taken as references for the integrated layouts.

According to the equilibrium curve, Fig. 1, the hydration reaction is preferred at high pressures for a given temperature. High inlet steam pressures considerably increase the conversion values, approaching complete conversion around 6 bars. An increase in conversion allows for greater thermal power during system discharge. However, operating at higher steam pressures requires high gas flow rates to fluidise the bed. Fig. 13 shows the effect of pressure on the conversion to hydration for a reactor with a diameter of 8 m and a height of 14 m.

4.3. Process integration

The previous subsections presented the definition of the optimum parameters for reactor operation. This section evaluates the

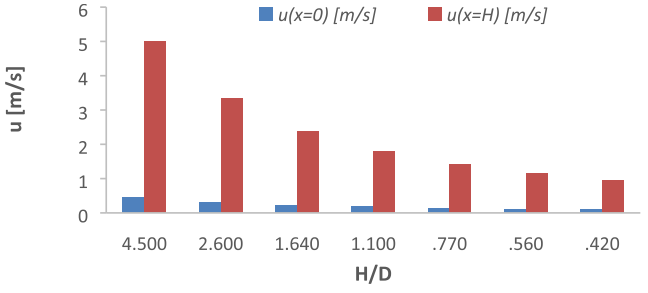

Fig. 10. Gas velocities at reactor inlet and outlet.

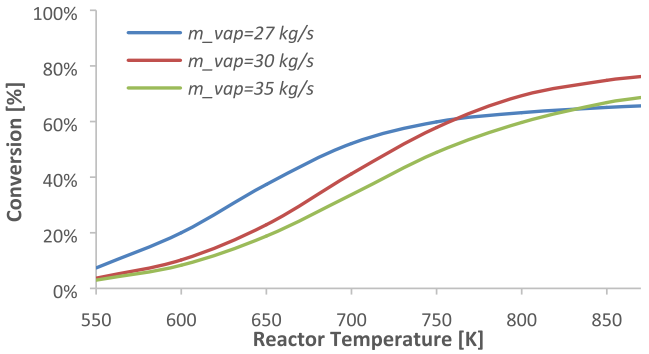

Fig. 11. CaO conversion as a function of reactor temperature.

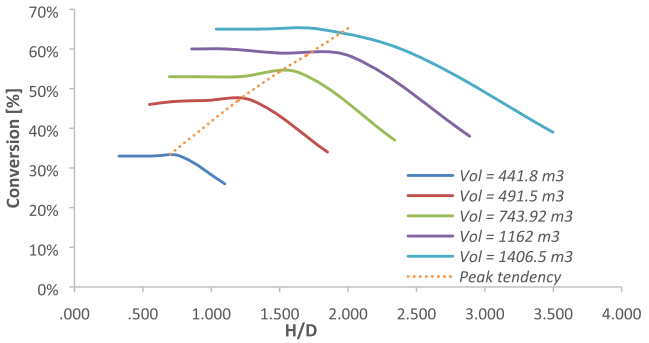

Fig. 12. Hydration conversion curves for different reactor volumes.

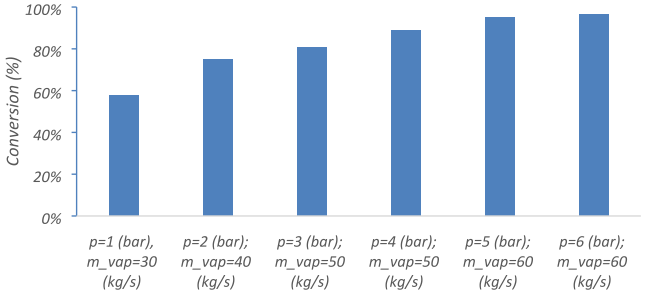

Fig. 13. FB solid conversion versus pressure (D = 8 m; H = 14 m).

performance of the integrated layouts, Fig. 5, which vary with hydration pressure. Two cases are considered from the previous discussion: ambient pressure (HY-1) and 6 bar (HY-2). The second case aims to maximise the power produced by the plant. However, the water consumption for fluidisation of the bed increases significantly. Each case will have an optimal thermal integration of the process.

For the thermal integration, a reactor of Dr = 10 m, Hr = 17 m was selected to maximise the heat released from the reactor to the transfer fluid. The operation at atmospheric pressure (HY-1) produces during the discharge phase 87.15 MWth to heat the process steam through an internal heat exchanger. Hydration at 6 bars (HY2) increases substantially the heat released, 126.5 MWth. The conversions obtained as the hydration reaction are favoured at high pressures but also increase the required cold water from the storage that must be overheated up to 550 K before entering the fluidised bed. To minimise it, a fraction of the steam coming out of the turbine downstream of the fluidised bed can be recirculated. For the thermal integration of this second case, a reactor of size Dr = 8 m, Hr = 15 m was selected. Table 2 shows the geometric characteristics of the reactor for both cases.

Table 3 and Table 4 show the mass and energy balances in the reactor.

Table 2
FB geometrical characteristics.

Description	Symbol	Units	INT-1		INT-2	
			HY	DEHY	HY	DEHY
Reactor Temperature	T_{FB}	K	750	800	750	800
Diameter FB	D_{FB}	m	10	10	8	8
Height FB	H_{FB}	m	17	17	15	15
Diameter pipe	d_t	mm	20	20	40	40
Distance pipe	a	mm	20	20	20	20
Pipe length	L_t	m	6.97	6.97	5.56	5.56
N° layer	N_s	–	25	298	41	175
N° pipes	N_t	–	4369	52083	3811	16297

Table 3
Mass flows in the reactor for the analysed integrations.

	Symbol	Units	Atmospheric pressure (hydration)		Pressurised - 6 bar (hydration)	
	Mass flow		HY-1	DEHY-1	HY-2	DEHY-2
Inlet	$m_{gas,\ total}$	kg/s	37	2.5	60	2.5
	$m_{gas,\ recirculated}$	kg/s	10.71	0	25.03	0
	$m_{gas,\ feed}$	kg/s	26.29	2.5	34.97	2.5
	m_{CaO}	kg/s	100	0	100	0
	$m_{Ca(OH)2}$	kg/s	0	100	0	100
Outlet	m_{gas}	kg/s	14.7	26.1	29.0	26.2
	m_{CaO}	kg/s	30.6	73.3	3.6	73.6
	$m_{Ca(OH)2}$	kg/s	91.7	3.1	127.4	2.7

Table 4
Energy balance for each integration scheme.

	Units	Atmospheric pressure (hydration)	Pressurised -6 bar-(hydration)
$W_{elect,hy}$	MW_e	23.16	36.7
$W_{elect,dehy}$	MW_e	38.96	53.5
$W_{feed,H2O\ hy}$	MW_{th}	76.8	101.9
$W_{feed,H2O\ dehy}$	MW_{th}	7.3	7.3
$W_{FB,hy}$	MW_{th}	87.15	126.5
$W_{FB,dehy}$	MW_{th}	187	187

Recirculating steam during the discharge phase reduces the energy used in preheating the cold water flow from the storage tank. Internal fluidised bed heat exchanger sizing aims to optimise performance during the charging and discharging phases of the system. During dehydration, the objective is to select HTF velocities and tube diameters to ensure a reactor temperature of at least 800 K for a high conversion level. Fig. 14 shows the reactor temperature as a function of the HTF velocity and pipe diameters for different reactor aspect ratios. It shows that achieving the temperature objective with high velocities of the fluid inside the tubes is possible. High velocities imply high-pressure drops inside the tubes, increasing heat transfer fluid pumping costs. For the hydration phase,

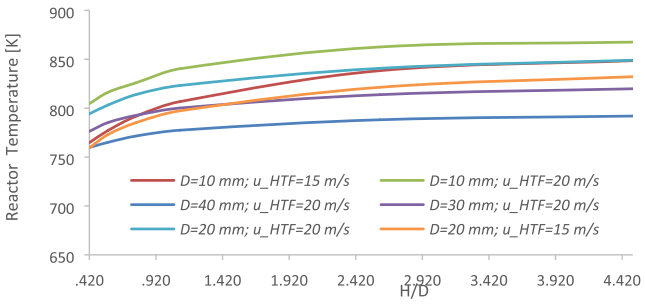

Fig. 14. Reactor temperature as a function of tube diameter and HTF velocity.

the aim is to size the exchanger according to the operating conditions of the steam cycle.

The study of the heat exchanger network aims to thermally integrate the different streams of the system, to minimise the heating and cooling consumption. The optimisation was carried out by the pinch analysis [45] by using the Aspen Energy Analyser tool to optimise the energy plant for both thermal integrations. The inlet and outlet temperatures of the hot and cold streams are considered for the analysis of their thermal integration by heat exchangers. During hydration, the cold current of the water from storage that must be brought to the superheated steam limits the thermal integration, as it is the most energy-intensive current in the entire system. Figs. 15 and 16 show the balanced composite curves and the grand composite curves obtained for the second thermal integration during both the charging and discharging phases of the system, respectively.

Table 5 shows the results obtained from the application of the pinch analysis. More heat exchangers must be installed during the dehydration reaction, although it is not necessary to cool the solids leaving the reactor, unlike during the charging phase of the system. The heat exchange surfaces used during dehydration are high due to the high steam flow rates produced during the reaction.

4.4. Performance parameters

In this section, the two integrations are compared using the following relevant parameters to evaluate the efficiency of the cycle. These parameters are:

– Power block efficiency. $W_{el,PB}$ represents the electrical power produced in the power cycle, while $W_{th,heaters}$ is the heat output required by the steam cycle heat exchangers. It integrates both hydration and dehydration periods, Eq. (11):

$$\eta_{PB} = \frac{W_{el,PB}}{W_{th,heaters}} \tag{11}$$

– Overall efficiency, defined as the ratio of the total electrical power produced by the power cycle to the thermal power input to the system, Eq. (12):

$$\eta_{tot} = \frac{W_{el,tot}}{Q_{solar}} = \frac{W_{el,HY} + W_{el,DEHY}}{Q_{solar}} \tag{12}$$

– Round trip efficiency is the ratio between the heat released by the storage system during discharge (heat provided by the fluid-bed reactor) and the heat required by the system during the charging phase, Eq. (13).

$$\eta_{RT} = \frac{Q_{hy}}{Q_{dehy}} \tag{13}$$

It excludes any type of thermal integration, such as the preheating line at the entrance to the reactor. Round-trip efficiencies reach values of 47 % in the first case while rising to 68 % with the second integration.

– Solid conversion. It is defined as Eq.14:

$$\chi = \frac{F_{Ca,in} - F_{Ca,out}}{F_{Ca,in}} \tag{14}$$

$F_{Ca,in}$ represents the molar flow rate (of hydroxide or calcium oxide, depending on whether it is hydration or dehydration) entering the reactor, meanwhile $F_{Ca,out}$ is the molar flow rate at the exit of the reactor. The cyclability and hence the reversibility of the reaction are functions of this parameter. When this parameter is closer to one, less solid replenishment is required.

– Water Consumption. The choice of using superheated steam instead of nitrogen gas, on the one hand, simplifies the plant scheme by eliminating steam/nitrogen separation; on the other hand, it increases the heat demand for preheating the water from the storage tank. Therefore, the following parameters are defined:

$$\xi = \frac{W_{th,feed\ H2O}}{W_{HY}} \tag{15}$$

$$V = \frac{m_{vap,converted}}{m_{vap,used}} \tag{16}$$

The first number indicates the energy consumption of the water used to heat the steam compared to the heat released during the hydration reaction. In both cases, the value of ξ is around 0.81/0.88, which shows that the process is very energy intensive. The second number represents the ratio of the mass flow rate of steam converted during the hydration reaction to the total flow rate required to fluidise the fluidised bed.

Fig. 17 compares and summarises the performance of the two configurations based on these parameters.

The indicators in Fig. 17 show that the second integration is overall successful compared to the first one. The performance indexes according to Equations (3)–(8). Clear improvements can be seen in the round-trip yield, the total yield, and the conversion value achieved during calcium oxide hydration.

These values are considered for the economic evaluation in the next section. The system charging phase, which presents higher costs than the discharging phase, was taken as the reference for LCOE calculation.

5. Economic analysis

The economic analysis is developed considering the integration

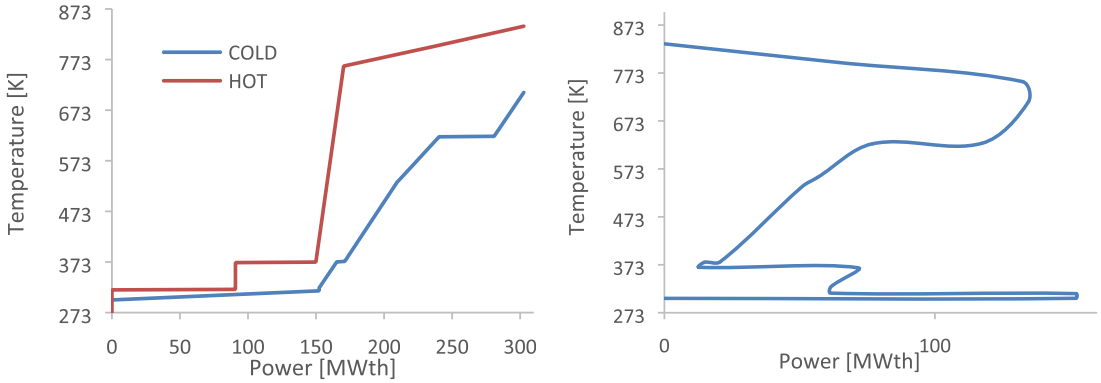

Fig. 15. a. BCC for Dehydration 2nd Thermal Integration Figgure 15b: GCC for Dehydration 2nd thermal integration.

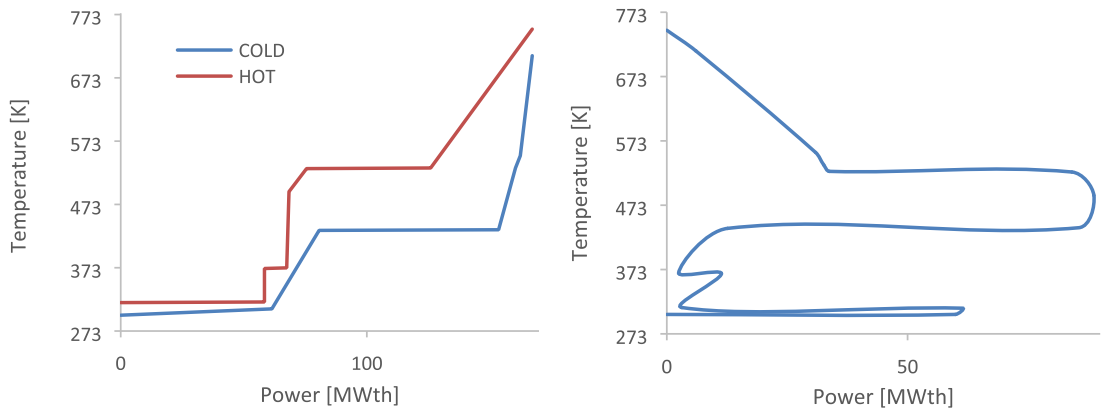

Fig. 16. a: BCC for Hydration 2nd Thermal Integration. b: GCC for Hydration 2nd thermal integration.

Table 5
Global results from the pinch analysis in the heat exchangers.

Stage/ Process	Number Heat Exchangers	A_{tot} [m^2]	Power [MW_{th}]
HY-1			
solid/fluid	3	3034	52
fluid/fluid	5	53511	87
DEHY-1			
fluid/fluid	10	80189	235.2
HY-2			
solid/fluid	4	3110	46.8
fluid/fluid	5	62648	118.9
DEHY-2			
fluid/fluid	10	110000	300

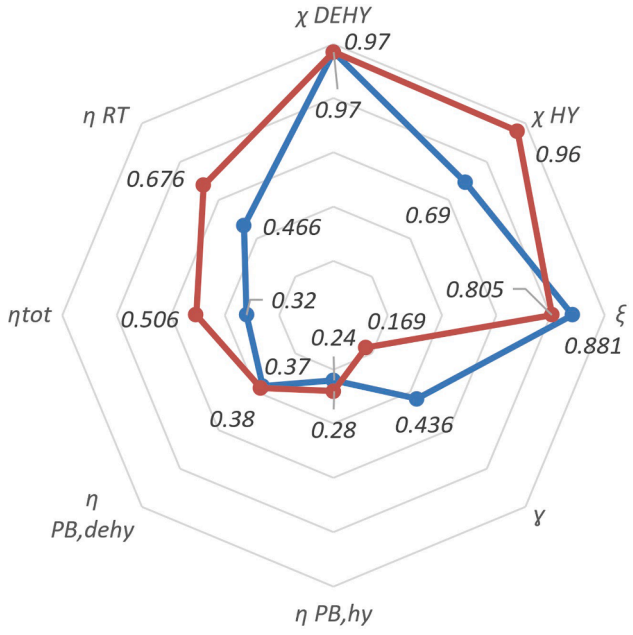

Fig. 17. Comparison of the main parameters of the two layouts: case 1 (BLUE) and case 2 (RED). (For interpretation of the references to colour in this figure legend, the reader is referred to the web version of this article.)

within a tower solar power plant. Investment costs show an apparent increase in the second integration due to the additional turbine and a more complex Heat Exchangers Network (HEN).

5.1. Capital investment costs

Capital investment costs are divided into four groups: solar block, power block, storage and heat exchangers network. Table 6 summarises the main hypotheses in the estimation of capital investment costs. Fig. 18 shows the estimated capital costs for the three plant sections that vary in the analysis. The solar block is considered constant.

The breakdown of capital costs within the whole solar concentration plant is consistent with that of a typical similar-sized plant operating with molten salt technology (Table 7).

The investment cost for the first integration was 4169.7 $/kWe, considering an average power produced of 31.06 MWe, while for the second integration, the specific investment cost is lowered to 3248.2 $/kWe considering an average power of 45.1 MWe.

5.2. LCOE index analysis

The Levelised Cost of Energy (LCOE) allows alternative technologies to be compared when different scales of operation, different investments, and operating periods exist. For this work, the simple LCOE calculation model, sLCOE, is used, Eq. (17), providing a metric that compares the combination of capital costs, O&M, performance, and fuel costs. It does not include financing issues, discount issues, future replacement or degradation costs, etc., which would need to be included for more complex analysis in specific scenarios.

$$sLCOE = \frac{CC \cdot CRF + O\&M_{fix}}{8760 \cdot CF} + F_{cost} \cdot HR + O\&M_{var} \quad (17)$$

The assumptions for calculating the LCOE are presented in Table 8.

Fig. 19 shows the LCOE trend as a function of the plant operating period. After about 20 years, LCOE stabilises at a fairly low value compared to other energy storage options.

Fig. 20 shows the LCOE results for each integration as a function of the number of possible replenishments the system needs in an operational year. The LCOE values were calculated assuming a system lifetime of 25 years. In 2019, the LCOE of a concentrating solar power plant was 182 $/MWh [9], while the results of the $Ca(OH)_2/CaO$ technology operating, however, with a fixed bed obtained an LCOE of 141 $/MWh [27]. The results obtained show the interest of the approach presented in this paper, although highly dependent on the material behaviour.

6. Conclusions

This study evaluated the techno-economic feasibility of a

Table 6
Esimated capital investment costs.

Heliostat Field & Tower Receiver	Units	Cost estimation	Reference
Site Preparation	$\$/m^2$	8.25	[46]
Mirrors	$\$/m^2$	21.45	[46]
Drivers	$\$/m^2$	39.4	[46]
Structure & fundation	$\$/m^2$	36.75	[46]
Controls	$\$/m^2$	0.4	[46]
Installation (wiring/foundation labour)	$\$/m^2$	13.5	[46]
Tower	$\$/m^2$	$90000^{(*)}$	[47]
Receiver	$\$/kW_{th}$	125	[48]

Storage Block	Units	Cost estimation	Reference
Solids Storage Tank	$\$/kW_{th}$	6.00	[48]
Foundations	$\$/kW_{th}$	0.7	[48]
Particle media	$\$/kW_{th}$	9.08	[48]
Piping/valves	$\$/kW_{th}$	1.00	[48]
Controls and Instrumentation	$\$/kW_{th}$	0.5	[48]
Spare parts and other direct costs	$\$/kW_{th}$	1.0	[48]
Contingency	$\$/kW_{th}$	4.00	[48]
H2O Storage Tank	$\$/m^3$	100	[42]
Ca(OH)$_2$ material	\$/ton	150	[42]
Fluidised bed	\$	$IC_{FB} = 106200\left(V^{(*)}_{Reactor}\right)^{0.5}$	[49]
Cyclone	\$	$IC_{cyclone} = 3.98{\cdot}10^{-9}\left(D^{(*)}_{cy}\right)^2 + 2.73{\cdot}10^{-6}D_{cy} + 1.6{\cdot}10^{-2}$	[50]

Power Block	Units	Cost estimation	Reference
Turbine	\$	$IC_{SRC\ turb} = 4125(W_{turb})^{0.7}\left[1+\left(\frac{0.05}{1-\eta_{is.turb}}\right)^3\right]\left[1+\exp\left(\frac{Tin^{(*)}-866}{10.42}\right)\right]$	[49]
Pump	\$	$IC_{SRC\ pump} = 750(W_{pump})^{0.71}\left(1+\frac{0.2}{1-\eta_{is.pump}}\right)$	[49]
Air Cooler	\$	$IC_{Air\ cooler} = UA_{Air\ cooler}{\cdot}c^{(*)}$	[49]

	UA [W/K]	$5{\cdot}10^3$	$3{\cdot}10^4$	$1{\cdot}10^5$	$3{\cdot}10^5$	$1{\cdot}10^6$
c [\$-K/W]	**Regenerator**	5.89	1.31	1.22	1.03	0.94
	Air cooler	9.66	3.05	1.65	1.04	1.27

Heat Exchanger Network		Cost estimation	Reference
Fluid/Fluid Heat Exchanger	\$	$IC_{fluid-fluid} = 3197{\cdot}A^{0.67}P^{0.28(*)}$	[49]
Solid/Fluid Heat Exchanger	\$	$IC_{fluid-solid} = 18.48{\cdot}(UA)^{0.67}P^{0.28(*)}$	[49]

(*) For this study an approximate value of 90000 \$/m is used for typical tower heights of about 200 m. It results in total tower costs of 20 Mio \$, which is between the values of [36] and [36].
(*) $V_{Reactor}$ is expressed in.m^3
(*) D_{cy} is expessed in mm.
(*) T_{in} is the vapor inlet temperature and is expressed in [K].
(*) 'c' is the normalised cost value calculated by linear interpolation of the corresponding UA values (product between global heat transfer coefficient and exchange surface) with the data in the table.
(*) p is the operative pressure.

thermochemical storage system using the reversible Ca(OH)$_2$/CaO reaction. The two reaction steps, one of charge and the other of discharge, take place within a fluidised bed reactor using superheated steam at 550 K as gas and reagent. The present work proposes a detailed dimensioning of the fluidised bed and the storage block to evaluate the possibility of their integration within a concentrating solar power plant, providing relevant insights into the integration process. A configuration with a single reactor reduces costs and can improve the competitiveness of the concept. However, as the sensitivity analysis results show, the design and operation of the two different reaction steps within the same fluidised bed are challenging. The Ca(OH)$_2$ dehydration reaction show almost complete conversions (thus allowing good cyclicity), which can be achieved at reactor temperatures of around 800 K. This phase requires high HTF flow rates to keep the reactor operating. However, low steam flow rates are required to fluidise the bed, thus reducing the heat demand needed for reaching the input design conditions. The hydration reaction shows greater limitations in terms of CaO conversion. The use of pressurised steam is shown to be of interest in terms of reaction performance, but at the same time, the high steam flow rates compromise some of the benefits. For the analysed layouts, a clear improvement in the performance parameters is obtained in the second configuration compared to the first. For the first integration, a value of the effective stored energy density of 242.5 kWh/m^3 was obtained, while this value increased to 352 kWh/m^3 for the second layout.

The economic analysis shows the feasibility of a potential plant using the proposed technology. The specific investment costs were competitive compared to those of current molten salt technology. The analysed configurations presented an estimated investment cost of 4169.7 \$/kWe and 3284.2 \$/kWe, clearly below the current values for a molten salt plant of similar size 6200/6400 \$/kWe. The values of the LCOE index also show the economic interest of the system, although highly dependent on material behaviour and performance degradation.

The simplifications adopted during the choice of the model suggest future developments that may concern a more detailed sizing of the exchanger network with particular attention to solid–gas heat exchange. In addition, a more precise fluid dynamic analysis simulating the

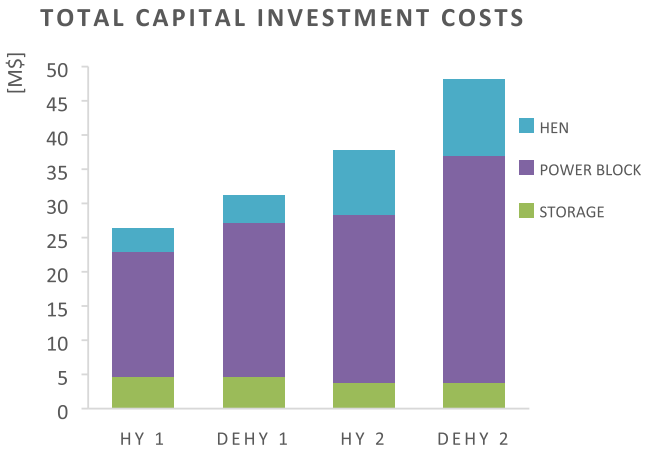

Fig. 18. Investment costs related to storage, power block and heat exchangers network for two integrations.

Table 7
Percentages of the components in the capital costs for the two layouts.

	Units	INT-1	INT-2
Receiver	%	32.1	28.3
Heliostats field	%	43.9	38.8
Storage	%	3.6	2.5
Power Block	%	17.4	22.7
HEN	%	3.1	7.6

Table 8
Input data for economic assessment.

	Units	INTEGRATION-1	INTEGRATION-2
Financial			
Period	Years	25	25
Discount Rate	%	3	3
Renewable System Cost and Performance			
Capital Cost	$/kW$_e$	4013	3017
Capacity factor	%	45.2	45.2
Fixed O&M	$/Kw	65	65
Variable O&M	$/MWh	3.5	3.5
Electricity cost			
Electricity price	c$/kWh	12	12
Cost escalation rate	%	0.25	0.25

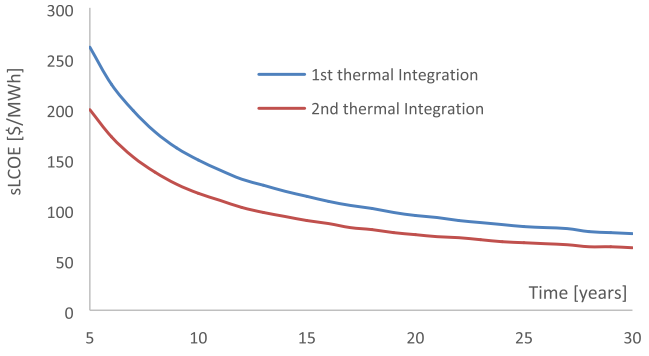

Fig. 19. Simple Levelized Cost of Renewable Energy vs time.

reaction and heat exchange between the solid vapour inside the fluidised bed and the operating fluid inside the exchanger tubes would be relevant for accurately determining the heat exchange coefficients. Finally, the

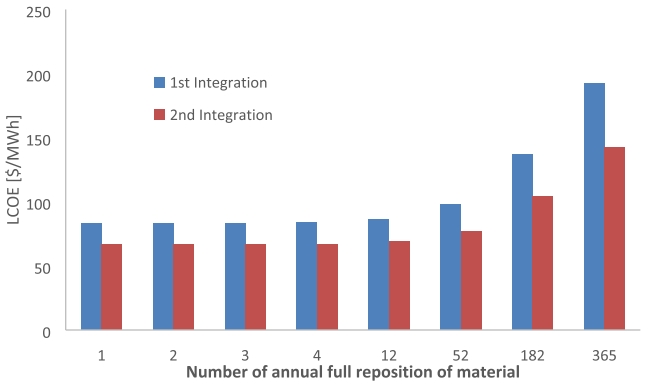

Fig. 20. LCOE as a function of the number of fresh material replenishments.

transient thermal study between the charging and discharging phases would lead to a complete view of the possible problems inherent in this technology. These problems could be solved by integrating existing and established technologies. Of particular interest would be an integrated study of the proposed technology with calcium looping technology (carbonation and calcination of carbon dioxide) operating at higher temperatures.

Declaration of Competing Interest

The authors declare the following financial interests/personal relationships which may be considered as potential competing interests: Ricardo Chacartegui, Jose A Becerra reports financial support was provided by Regional Government of Andalucia, Junta de Andalucia. Ricardo Chacartegui, Jose A Becerra reports financial support was provided by European Regional Development Fund.

Data availability

Data will be made available on request.

Acknowledgment

This work was partially funded by the project 'Sistema de almacenamiento termóquímico de energía para plantas solares de concentración- SunStorCa(OH)$_2$, reference P18-RT-1044, by the Regional Government of Andalucia, Junta de Andalucia, and FEDER Regional European Funds.

References

[1] National Renewable Energy Laboratory (NREL), Concentrating Solar Power Projects, 2017.
[2] M. Liu, N.H. Steven Tay, S. Bell, M. Belusko, R. Jacob, G. Will, W. Saman, F. Bruno, Review on concentrating solar power plants and new developments in high temperature thermal energy storage technologies, Renew. Sustain. Energy Rev. 53 (2016) 1411–1432, https://doi.org/10.1016/j.rser.2015.09.026.
[3] D. Kearney, B. Kelly, U. Herrmann, R. Cable, J. Pacheco, R. Mahoney, H. Price, D. Blake, P. Nava, N. Potrovitza, Engineering aspects of a molten salt heat transfer fluid in a trough solar field, Energy. 29 (2004) 861–870, https://doi.org/10.1016/S0360-5442(03)00191-9.
[4] X. Song, G. Zhang, H. Tan, L. Chang, L. Cai, G. Xu, Z. Deng, Z. Han, Review on Thermophysical Properties and Corrosion Performance of Molten Salt in High Temperature Thermal Energy Storage, IOP Conf. Series: Earth Environ. Sci. 474 (2020) 052071. https://doi.org/10.1088/1755-1315/474/5/052071.
[5] A.G. Fernández, J. Gomez-Vidal, E. Oró, A. Kruizenga, A. Solé, L.F. Cabeza, Mainstreaming commercial CSP systems: A technology review, Renew. Energy 140 (2019) 152–176, https://doi.org/10.1016/J.RENENE.2019.03.049.
[6] Irena, Renewable energy technologies: cost analysis series Wind Power, Power Generation Technol. 1 (2012) 223–242, https://doi.org/10.1016/B978-0-08-098330-1.00011-9.
[7] A. Carro, R. Chacartegui, C. Ortiz, J. Carneiro, J.A. Becerra, Energy Storage System based on transcritical CO2 cycles and geological storage, Appl. Therm. Eng. 193 (2021), 116813, https://doi.org/10.1016/j.applthermaleng.2021.116813.

[8] B. Zalba, J.M. Marín, L.F. Cabeza, H. Mehling, Review on thermal energy storage with phase change: Materials, heat transfer analysis and applications, Appl. Therm. Eng. 23 (2003) 251–283, https://doi.org/10.1016/S1359-4311(02)00192-8.

[9] A. Sharma, V.V. Tyagi, C.R. Chen, D. Buddhi, Review on thermal energy storage with phase change materials and applications, Renew. Sustain. Energy Rev. 13 (2) (2009) 318–345.

[10] A.J. Carrillo, J. González-Aguilar, M. Romero, J.M. Coronado, Solar Energy on Demand: A Review on High Temperature Thermochemical Heat Storage Systems and Materials, Chem. Rev. 119 (2019) 4777–4816, https://doi.org/10.1021/acs.chemrev.8b00315.

[11] P. Pardo, A. Deydier, Z. Anxionnaz-Minvielle, S. Rougé, M. Cabassud, P. Cognet, A review on high temperature thermochemical heat energy storage, Renew. Sustain. Energy Rev. 32 (2014) 591–610, https://doi.org/10.1016/j.rser.2013.12.014.

[12] T. Yan, R.Z. Wang, T.X. Li, L.W. Wang, I.T. Fred, A review of promising candidate reactions for chemical heat storage, Renew. Sustain. Energy Rev. 43 (2015) 13–31, https://doi.org/10.1016/j.rser.2014.11.015.

[13] F. Schaube, I. Utz, A. Wörner, H. Müller-Steinhagen, De- and rehydration of Ca(OH)2in a reactor with direct heat transfer for thermo-chemical heat storage. Part B: Validation of model, Chem. Eng. Res. Des. 91 (2013) 865–873, https://doi.org/10.1016/j.cherd.2013.02.019.

[14] I. Fujii, K. Tsuchiya, M. Higano, J. Yamada, Studies of an energy storage system by use of the reversible chemical reaction: CaO + H2O ⇌ Ca(OH)2, Sol. Energy 34 (1985) 367–377, https://doi.org/10.1016/0038-092X(85)90049-0.

[15] H. Ogura, R. Shimojyo, H. Kage, Y. Matsuno, A.S. Mujumdar, Simulation of hydration/dehydration of CaO/Ca(OH)2 chemical heat pump reactor for cold/hot heat generation, Drying Technol. 17 (7-8) (1999) 1579–1592.

[16] A. Ong'iro, V.I. Ugursal, A.M. Al Taweel, J.D. Walker, Modeling of heat recovery steam generator performance, Appl. Therm. Eng. 17 (1997) 427–446, https://doi.org/10.1016/S1359-4311(96)00052-X.

[17] K. Risthaus, I. Bürger, M. Linder, M. Schmidt, Numerical analysis of the hydration of calcium oxide in a fixed bed reactor based on lab-scale experiments, Appl. Energy 261 (2020) 114351.

[18] M. Schmidt, C. Szczukowski, C. Roßkopf, M. Linder, A. Wörner, Experimental results of a 10 kW high temperature thermochemical storage reactor based on calcium hydroxide, Appl. Therm. Eng. 62 (2014) 553–559, https://doi.org/10.1016/J.APPLTHERMALENG.2013.09.020.

[19] S. Rougé, Y.A. Criado, O. Soriano, J.C. Abanades, Continuous CaO/Ca(OH)2 fluidised bed reactor for energy storage: First experimental results and reactor model validation, Ind. Eng. Chem. Res. 56 (2017) 844–852, https://doi.org/10.1021/acs.iecr.6b04105.

[20] P. Pardo, Z. Anxionnaz-Minvielle, S. Rougé, P. Cognet, M. Cabassud, Ca(OH)2/CaO reversible reaction in a fluidised bed reactor for thermochemical heat storage, Sol. Energy 107 (2014) 605–616, https://doi.org/10.1016/J.SOLENER.2014.06.010.

[21] M. [German A.C.– D.L.R. e. V. "Schmidt I. of T.T.L.H. 51147 Köln (Germany)]", C. [German A.C.– D.L.R. e. V. "Szczukowski I. of T.T.L.H. 51147 Köln (Germany)]", C. "Roßkopf, M. "Linder, A. [German A.C.– D.L.R. e. V. "Wörner I. of T.T.P. 38 70569 Stuttgart (Germany)]", Experimental results of a 10 kW high temperature thermochemical storage reactor based on calcium hydroxide, Appl. Therm. Eng. 62 (2014) 553–559. https://doi.org/10.1016/j.applthermaleng.2013.09.020.

[22] A. Cosquillo Mejia, S. Afflerbach, M. Linder, M. Schmidt, Experimental analysis of encapsulated CaO/Ca(OH)2 granules as thermochemical storage in a novel moving bed reactor, Appl. Therm. Eng. 169 (2020), 114961, https://doi.org/10.1016/J.APPLTHERMALENG.2020.114961.

[23] Q. Xu, J. Sun, Z. Ma, R. Xie, J. Wei, Influences of variable porosity on CaO/Ca(OH)2 thermochemical energy storage characteristics in direct/indirect heated reactor, Appl. Therm. Eng. 208 (2022), 118231, https://doi.org/10.1016/J.APPLTHERMALENG.2022.118231.

[24] L. Dai, X.F. Long, B. Lou, J. Wu, Thermal cycling stability of thermochemical energy storage system Ca(OH)2/CaO, Appl. Therm. Eng. 133 (2018) 261–268, https://doi.org/10.1016/J.APPLTHERMALENG.2018.01.059.

[25] C. Ortiz, J.M. Valverde, R. Chacartegui, L.A. Perez-Maqueda, P. Giménez, The Calcium-Looping (CaCO3/CaO) process for thermochemical energy storage in Concentrating Solar Power plants, Renew. Sustain. Energy Rev. 113 (2019) 109252.

[26] A. Bayon, R. Bader, M. Jafarian, L. Fedunik-Hofman, Y. Sun, J. Hinkley, S. Miller, W. Lipiński, Techno-economic assessment of solid–gas thermochemical energy storage systems for solar thermal power applications, Energy. 149 (2018) 473–484, https://doi.org/10.1016/j.energy.2017.11.084.

[27] Y.A. Criado, M. Alonso, J.C. Abanades, Z. Anxionnaz-Minvielle, Conceptual process design of a CaO/Ca(OH)2 thermochemical energy storage system using fluidised bed reactors, Appl. Therm. Eng. 73 (2014) 1087–1094, https://doi.org/10.1016/J.APPLTHERMALENG.2014.08.065.

[28] E. Tapachès, D. Salas, M. Perier-Muzet, S. Mauran, D. Aussel, N. Mazet, The value of thermochemical storage for concentrated solar power plants: Economic and technical conditions of power plants profitability on spot markets, Energy Convers. Manage. 198 (2019) 111078.

[29] U. Pelay, L. Luo, Y. Fan, D. Stitou, C. Castelain, Integration of a thermochemical energy storage system in a Rankine cycle driven by concentrating solar power: Energy and exergy analyses, Energy. 167 (2019) 498–510, https://doi.org/10.1016/j.energy.2018.10.163.

[30] U. Pelay, C. Azzaro-Pantel, Y. Fan, L. Luo, Life cycle assessment of thermochemical energy storage integration concepts for a concentrating solar power plant, Environ. Prog. Sustainable Energy 39 (2020), e13388, https://doi.org/10.1002/EP.13388.

[31] M.N. Azpiazu, J.M. Morquillas, A. Vazquez, Heat recovery from a thermal energy storage based on the Ca(OH)2/CaO cycle, Appl. Therm. Eng. 23 (2003) 733–741, https://doi.org/10.1016/S1359-4311(03)00015-2.

[32] C. Ortiz, J.M. Valverde, R. Chacartegui, L.A. Pérez-Maqueda, P. Gimenez-Gavarrell, Scaling-up the Calcium-Looping Process for CO2 Capture and Energy Storage, Kona Powder Part. J. 38 (2021) 189–208, https://doi.org/10.14356/KONA.2021005.

[33] F. Schaube, L. Koch, A. Wörner, H. Müller-Steinhagen, A thermodynamic and kinetic study of the de- and rehydration of Ca(OH)2 at high H2O partial pressures for thermo-chemical heat storage, Thermochim. Acta 538 (2012) 9–20, https://doi.org/10.1016/J.TCA.2012.03.003.

[34] J.A.C. Samms, B.E. Evans, Thermal dissociation of Ca(OH)2 at elevated pressures, J. Appl. Chem. 18 (1968) 5–8, https://doi.org/10.1002/JCTB.5010180102.

[35] I. Barin, Thermochemical data of pure substances VCH, Weinheim, 1989.

[36] Y.A. Criado, M. Alonso, J.C. Abanades, Z. Anxionnaz-Minvielle, Conceptual process design of a CaO/Ca(OH)2thermochemical energy storage system using fluidised bed reactors, Appl. Therm. Eng. 73 (2014) 1087–1094, https://doi.org/10.1016/j.applthermaleng.2014.08.065.

[37] Y.A. Criado, M. Alonso, J.C. Abanades, Kinetics of the CaO/Ca(OH)2 hydration/dehydration reaction for thermochemical energy storage applications, Ind. Eng. Chem. Res. 53 (2014) 12594–12601, https://doi.org/10.1021/ie404246p.

[38] H. Ogura, T. Yamamoto, H. Kage, Y. Matsuno, M. as,, Effects of heat exchange condition on hot air production by a chemical heat pump dryer using CaO/H2O/Ca(OH)(2) reaction, Chem. Eng. J. 86 (2002) 3–10, https://doi.org/10.1016/S1385-8947(01)00265-0.

[39] A. Cosquillo Mejia, S. Afflerbach, M. Linder, M. Schmidt, Experimental analysis of encapsulated CaO/Ca(OH)2 granules as thermochemical storage in a novel moving bed reactor, Appl. Therm. Eng. 169 (2020) 114961.

[40] H. Zhang, J. Baeyens, G. Cáceres, J. Degrève, Y. Lv, Thermal energy storage: Recent developments and practical aspects, Prog. Energy Combust. Sci. 53 (2016) 1–40, https://doi.org/10.1016/j.pecs.2015.10.003.

[41] U. Pelay, L. Luo, Y. Fan, D. Stitou, Dynamic modeling and simulation of a concentrating solar power plant integrated with a thermochemical energy storage system, J. Storage Mater. 28 (2020), 101164, https://doi.org/10.1016/j.est.2019.101164.

[42] X. Peng, M. Yao, T.W. Root, C.T. Maravelias, Design and analysis of concentrating solar power plants with fixed-bed reactors for thermochemical energy storage, Appl. Energy 262 (2020), 114543, https://doi.org/10.1016/j.apenergy.2020.114543.

[43] A. Haider, O. Levenspiel, Drag coefficient and terminal velocity of spherical and nonspherical particles, Powder Technol. 58 (1989) 63–70, https://doi.org/10.1016/0032-5910(89)80008-7.

[44] U. Muschelknautz, E. Muschelknautz, Abscheideleistung von Rückführzyklonen in Wirbelschichtfeuerungen, VGB Kraftwerkstech. 79 (1999) 58–63.

[45] F. Marechal, Process Integration and Improvement, Exergy, Energy System Analysis, and Optimisation – Vol. I - Process Integration and Improvement. I (2009).

[46] CO. National Renewable Energy Laboratory. Golden, System Advisor Model Version 2017.1.17 (SAM 2017.1.17), (n.d.).

[47] S. Dieckmann, J. Dersch, S. Giuliano, M. Puppe, E. Lüpfert, K. Hennecke, R. Pitz-Paal, M. Taylor, P. Ralon, LCOE reduction potential of parabolic trough and solar tower CSP technology until 2025, in: AIP Conference Proceedings, American Institute of Physics Inc., 2017, https://doi.org/10.1063/1.4984538.

[48] C.K. Ho, A review of high-temperature particle receivers for concentrating solar power, Appl. Therm. Eng. 109 (2016) 958–969, https://doi.org/10.1016/j.applthermaleng.2016.04.103.

[49] U. Tesio, E. Guelpa, V. Verda, Integration of ThermoChemical Energy Storage in Concentrated Solar Power. Part 2: comprehensive optimisation of supercritical CO2 power block, Energy Convers. Manage.: X. 6 (2020), 100038, https://doi.org/10.1016/j.ecmx.2020.100038.

[50] E. De Lena, M. Spinelli, M. Gatti, R. Scaccabarozzi, S. Campanari, S. Consonni, G. Cinti, M.C. Romano, Techno-economic analysis of calcium looping processes for low CO 2 emission cement plants, Int. J. Greenhouse Gas Control (2019) 244–260, https://doi.org/10.1016/j.ijggc.2019.01.005.